Chemical Science

ROYAL SOCIETY OF CHEMISTRY

EDGE ARTICLE

Cite this: *Chem. Sci.*, 2024, **15**, 11564

All publication charges for this article have been paid for by the Royal Society of Chemistry

A tricycloquinazoline based 2D conjugated metal–organic framework for robust sodium-ion batteries with co-storage of both cations and anions†

Dan Chen,‡[ac] Linqi Cheng,‡[b] Weiben Chen,‡[ac] Heng-Guo Wang, *[b] Fengchao Cui[b] and Long Chen *[a]

Received 7th February 2024
Accepted 18th June 2024

DOI: 10.1039/d4sc00932k

rsc.li/chemical-science

There is growing interest in 2D conjugated metal–organic frameworks (2D *c*-MOFs) for batteries due to their reversible redox chemistry. Nevertheless, currently reported 2D *c*-MOFs based on n-type ligands are mostly focused on the storage of cations for batteries. Herein, we successfully synthesize nitrogen-rich and electron-deficient p-type ligand-based $Ni_3(HATQ)_2$ assembled from 2,3,7,8,12,13-hexaaminotricycloquinazoline (HATQ), and the ion co-storage feature of cations and anions in sodium ion batteries (SIBs) is demonstrated for 2D *c*-MOFs for the first time. The redox chemistry from the p-type ligand and π–d hybridization center endows the $Ni_3(HATQ)_2$ cathode with high capacity and good rate performance, especially excellent capacity retention of 95% after 1000 cycles. These findings provide a promising avenue for the exploration of other p-type multidentate chelating ligands toward new 2D *c*-MOFs and expand the application of 2D *c*-MOFs in energy storage systems.

Introduction

The development of clean and sustainable energy sources is driving the progress of emerging energy storage devices and technologies, which would have the advantage of overcoming the ever-increasing cost of lithium-ion batteries (LIBs).[1–4] Among these technologies, sodium ion batteries (SIBs) are expected to become promising alternatives to lithium ion batteries (LIBs) due to their cost-effectiveness, comparable electrochemical performance and abundant sodium resources.[5,6] However, the common electrode materials that are suitable for LIBs may exhibit sluggish reaction kinetics and rapid capacity decay in SIBs due to the larger radius of Na^+ compared to Li^+.[7,8] In this context, organic electrode materials seem to be a promising candidate due to their flexible structure designability as well as their cost effectiveness and resource abundance. Unfortunately, their low electrical conductivity and high dissolution in electrolytes seriously reduce the utilization of redox active sites and cycle stability.[9,10] Therefore, the exploration of structurally adaptive and promising conductive electrode materials with multi-redox active sites for SIBs is highly desired.

As a distinct category of conductive coordination polymers (CCPs), two-dimensional conjugated metal–organic frameworks (2D *c*-MOFs) are constructed by coordination of transition-metal ions with planar conjugated ligands containing *ortho*-substituted functional groups (–OH, $–NH_2$, and SH, Fig. 1a and b).[11–16] The unique square-planar linkages (MX_4, M = metal) facilitate the delocalization of charge carriers in 2D conjugated networks, which immensely enhances electronic transport.[17–20] While a plethora of MO_4 linkage-based 2D *c*-MOFs have been explored, varying functional groups from –OH to $–NH_2$ and –SH in the same ligands usually result in tunable electrical conductivity and coordination ability due to the discrepancy in the atom radius and π–d hybridization between the ligands and transition-metal ions.[21–25] Specifically, several recent studies have demonstrated that MX_4 units based on benzene or triphenylene ligands can serve as crucial redox active centers.[26–28] Furthermore, redox-active ligands based on tetraminobenzoquinone and hexaazatrinaphthylene in 2D *c*-MOFs have been reported, which integrate dual-redox centers.[26,29–31] However, these reported MX_4 linked organic ligands are mainly based on n-type organic compounds that serve as electron acceptors with intercalation of cations, limiting high throughput screening of electrode materials. By comparison, tricycloquinazoline (TQ),[32–35] as a nitrogen-rich and electron-deficient heteroaromatic-conjugated ligand core, can not only increase the acidity of the coordination functional groups, resulting in higher crystalline 2D *c*-MOFs, but also act as a p-type organic compound that serves as the electron donor with intercalation of anions,[36] expanding the active charge carriers of 2D *c*-MOFs. Therefore, the integration of p-type TQ ligands can construct

[a]*State Key Laboratory of Supramolecular Structure and Materials, College of Chemistry, Jilin University, Changchun, 130012, China. E-mail: longchen@jlu.edu.cn*

[b]*Key Laboratory of Polyoxometalate and Reticular Material Chemistry of Ministry of Education, Faculty of Chemistry, Northeast Normal University, Changchun, 130024, China. E-mail: wanghg061@nenu.edu.cn*

[c]*Department of Chemistry, Tianjin Key Laboratory of Molecular Optoelectronic Science, Tianjin University, Tianjin, 300072, China*

† Electronic supplementary information (ESI) available. See DOI: https://doi.org/10.1039/d4sc00932k

‡ These authors contributed equally to this work.

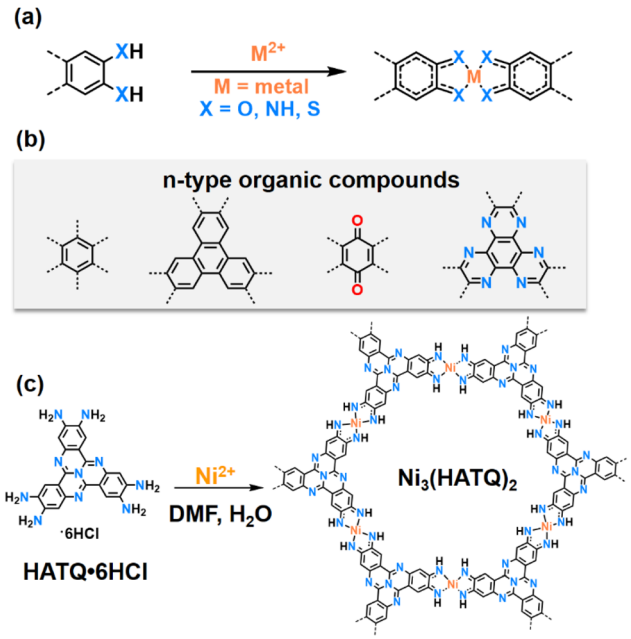

Fig. 1 The coordination of transition-metal ions with different planar conjugated ligands and design strategy of $Ni_3(HATQ)_2$. (a) The representative coordination process of square-planar transition-metal ions with *ortho*-substituted organic conjugated ligands. (b) The typical n-type organic structures in 2D *c*-MOFs. (c) The synthetic route of $Ni_3(HATQ)_2$.

artificial bipolar 2D *c*-MOFs that can achieve the co-storage of cations and anions. However, as far as we know, 2D *c*-MOFs based on p-type ligands as cathode materials for advanced SIBs with novel cation/anion co-storage modes have not been reported.

In this work, we reported the synthesis of hexaaminotricycloquinazoline (HATQ)-based 2D *c*-MOF $Ni_3(HATQ)_2$ (Fig. 1c) that acted as a bipolar active material for advanced SIBs for the first time. Interestingly, the bipolar framework material consists of n-type MN_4 active centers, aiming to store cations, and p-type TQ blocks, aiming to store anions. As expected, $Ni_3(HATQ)_2$ was then investigated as a cathode of SIBs, exhibiting a high reversible capacity of 115.1 mA h g^{-1}, good rate performance with 77.1 mA h g^{-1} at 2 A g^{-1}, and long-term cycling stability with 95% capacity retention after 1000 cycles, which is superior to its Ni_3(HITP)$_2$ (HITP = hexaiminotriphenylene) counterpart. In addition, all-organic SIBs were assembled by pairing the $Ni_3(HATQ)_2$ cathode with a sodium terephthalate anode, which shows the feasibility of practical application. Remarkably, the co-storage features of cations and anions were revealed by both experimental and theoretical investigations. These investigations may pave the way for the design and construction of novel 2D *c*-MOFs with the co-storage mode.

Results and discussion

HATQ was ingeniously designed and newly prepared in high yields (Schemes S1–S5†). More specifically, the pivotal hexabromotricycloquinazoline (HBTQ) precursor was first prepared through bromination and trimerization reactions. Subsequently, the diphenylmethanimine-substituted tricycloquinazoline was obtained by the Buchwald–Hartwig coupling reaction using HBTQ and diphenylmethanimine, followed by hydrolysis to yield brown precipitates (Fig. S1–S4†).[37] The chemical compositions of the target product were verified to be hexaaminotricycloquinazoline hexahydrochloride (HATQ·6HCl) by using ^{1}H and ^{13}C NMR, high-resolution mass spectra, elemental analysis, thermogravimetric analysis (TGA), and X-ray photoelectron spectroscopies (XPS) (Fig. S5–S8†).

$Ni_3(HATQ)_2$ was constructed by coordination of HATQ·6HCl with Ni^{2+} in square-planar geometry upon solvothermal synthesis using *N*,*N*-dimethylformamide (DMF) and water as the mixed solvent under basic conditions at 85 °C for three days (Fig. S9 and Scheme S6†). The resulting precipitate was thoroughly washed with *N*,*N*-dimethylacetamide, water, methanol and acetone, suggesting its solvent stability. Detailed characterization studies were performed to evaluate the fine structure of $Ni_3(HATQ)_2$. Fourier transform infrared (FT-IR) spectra showed that the featured peaks of amino (*ca.* 3190–3350 cm^{-1}) apparently disappeared (Fig. S10†). The peaks at *ca.* 505 and *ca.* 3630 cm^{-1} were assigned to Ni–N and –NH bands, respectively, indicating the formation of coordination bonds between Ni^{2+} and NH of the HATQ ligand.[38,39] Besides, the other characteristic peaks in the TQ core also existed in $Ni_3(HATQ)_2$, further suggesting successful formation of $Ni_3(HATQ)_2$. Meanwhile, the elemental compositions of $Ni_3(HATQ)_2$ were disclosed by XPS. As shown in Fig. S11,† these featured peaks in the full spectrum were assigned to be C, N, O and Ni elements. Among them, the existence of the O 1s peak in the spectrum may be attributed to trapped H_2O in the porous skeletons.[23,40–42] Compared to high-resolution C 1s and N 1s spectra of HATQ·6HCl in Fig. S8,† the Ni ion coordinated with N results in the evident change of binding energies in C (C–N) and N (N–C) of $Ni_3(HATQ)_2$. The absence of Cl^- signal peaks and extraneous Na^+ counterions suggests that $Ni_3(HATQ)_2$ is neutral.[23] Two characteristic peaks at 855.6 and 873.4 eV in the high-resolution spectra of the Ni element are assigned to Ni $2p_{3/2}$ and Ni $2p_{1/2}$ with evident satellite peaks at 860 and 880 eV, suggesting that the Ni element could be in the divalent state. Furthermore, the local structure of $Ni_3(HATQ)_2$ was investigated by X-ray absorption fine-structure (XAFS) using Ni foil and NiO as the reference.[43,44] As shown in Fig. 2a, the collected Ni K-edge X-ray absorption near edge structure (XANES) profile of $Ni_3(HATQ)_2$ resembled that of NiO and mismatched with Ni foil, suggesting the domination of the +2-oxidation state of Ni. Furthermore, the coordination environments of Ni in $Ni_3(HATQ)_2$, NiO and Ni foil were evaluated using wavelet transformed extended X-ray absorption fine structure (EXAFS) (Fig. S12c and S13†). The maximum peaks at *ca.* 3.3 $Å^{-1}$ of the *k*-space value and *ca.* 1.7 Å of the *R*-space value were close to that of Ni–O contribution in the NiO spectrum (Fig. S12b†), which was attributed to the Ni–N bonds, without apparent peaks of the Ni–Ni bond at *ca.* 2.2 Å of the *R*-space value, indicating the absence of residual metallic Ni clusters in $Ni_3(HATQ)_2$. Additionally, the coordinated bond parameters of $Ni_3(HATQ)_2$ were further investigated based on fitting of experimental Ni K-edge EXAFS oscillation $k^2\chi(k)$ as shown in

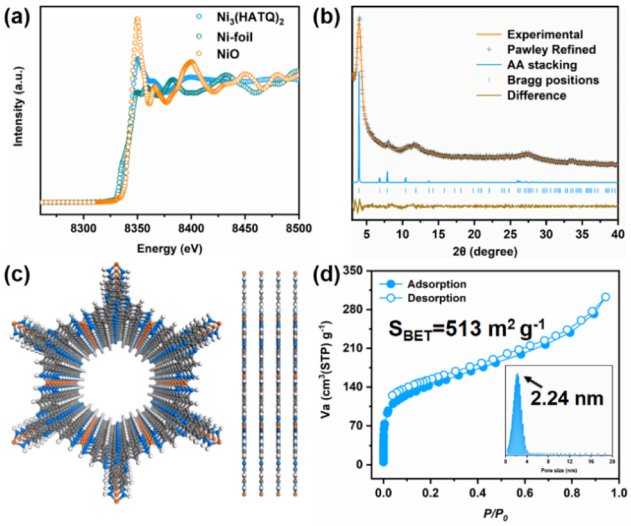

Fig. 2 Characterization of the valence state, crystallinity, simulated structure and porosity of $Ni_3(HATQ)_2$. (a) XANES of NiO, Ni foil and $Ni_3(HATQ)_2$. (b) Experimental and Pawley refined XRD profiles of $Ni_3(HATQ)_2$. (c) The structural model. (d) Nitrogen-sorption isotherms of $Ni_3(HATQ)_2$.

Fig. S12a and b.† The first coordination peak of $Ni_3(HATQ)_2$ with *ca.* 2.12 Å of the interatomic distances was ascribed to the Ni–N bond with an average coordination number of *ca.* 4.5 (Table S1†). Thus, the XAFS spectra strongly support the formation of square-planar NiN_4 coordination units in $Ni_3(HATQ)_2$. The crystalline structure of $Ni_3(HATQ)_2$ has been determined through a combination of powder X-ray diffraction (PXRD) measurements and theoretical simulation. The experimental PXRD profile of $Ni_3(HATQ)_2$ displays four distinct peaks at 4.00°, 8.05°, 10.60° and 27.55° which are assigned to be (100), (200), (210) and (001) facets, respectively (Fig. 2b). Meanwhile, the simulated XRD profile and the Pawley refined data of eclipsed AA stacking mode can match well with the experimental data, with a small difference (R_{wp} = 3.08% and R_p = 2.48%, Fig. 2c). The unit cell parameters for $Ni_3(HATQ)_2$ are determined to be $a = b = 25.91$ Å, $c = 3.42$ Å, $\alpha = \beta = 90°$, and $\gamma = 120°$. In contrast, the XRD profiles of staggered AB stacking mode cannot reproduce the experimental one (Fig. S14†). Furthermore, the permanent porosities of $Ni_3(HATQ)_2$ were evaluated using the nitrogen adsorption–desorption isotherm at 77 K (Fig. 2d). The Brunauer–Emmett–Teller surface area of $Ni_3(HATQ)_2$ was determined to be 513 $m^2\ g^{-1}$ and the pore size was calculated to be 2.24 nm, which matches perfectly with the theoretical value (2.24 nm).[20] As shown in Fig. S15,† the field emission scanning electron microscopy (FE-SEM) images exhibited nanorod-like morphology of $Ni_3(HATQ)_2$. Furthermore, the high-resolution transmission electron microscopy images exhibited distinct lattice fringes, with 2.08 nm of the corresponding channels being close to the theoretical and experimental pore size values (Fig. S16†). As shown in Fig. S17,† the solid-state ultraviolet diffuse reflection spectra of $Ni_3(HATQ)_2$ displayed broader absorption compared to the precursor, and the optical bandgap was calculated to be 1.52 eV using Tauc plots, which indicated that an extended π-conjugated skeleton is favorable for modulating the optical properties. Notably, the electrical conductivity is a unique identity of 2D *c*-MOFs. The conductivity value of bulk $Ni_3(HATQ)_2$ was 2.12 mS m^{-1} at room temperature, which is beneficial for electrochemical devices (Fig. S18†). Furthermore, thermogravimetric analysis revealed that the framework decomposes at *ca.* 400 °C (Fig. S19†), indicating good thermal stability.

For comparison, $Ni_3(HITP)_2$ was also synthesized and characterized (Scheme S7, Fig. S20 and S21†). As shown in Fig. S20,† $Ni_3(HITP)_2$ exhibited a feature of crystallinity. Additionally, elemental compositions of $Ni_3(HITP)_2$ were disclosed by XPS as shown in Fig. S21.† First, in the full spectrum, these featured peaks were assigned to be C, N, O and Ni elements. Similar to $Ni_3(HATQ)_2$, the existence of the O 1s peak may be attributed to trapped H_2O.[23,40–42] Two characteristic peaks at 855.5 and 872.7 eV in the high-resolution spectra of the Ni element are assigned to Ni $2p_{3/2}$ and Ni $2p_{1/2}$, suggesting that the Ni element could be in the divalent state.

Benefiting from its unique crystalline feature, $Ni_3(HATQ)_2$ is supposed to exhibit potential application in SIBs. First, coin-type half batteries were assembled using pure metallic sodium (counter electrode) and $Ni_3(HATQ)_2$ (cathode material) to evaluate the electrochemical performance. Cyclic voltammetry (CV) curves were measured at a scan rate of 0.1 mV s^{-1} with a voltage ranging from 1.0 to 3.6 V. As shown in Fig. 3a, the first CV curve showed a reductive peak at 1.57 V, which may be attributed to the reduction of the C=N bond in the coordination center, and two oxidation peaks at 1.63 and 2.45 V, which may be ascribed to the oxidation of C–N–Na. Distinct redox peaks at 2.73 and 3.21 V were manifested as anion desertion and insertion.[28] These results suggest multiple electron participation in charge and discharge processes.

Meanwhile, the redox peaks became more stable with increasing scan cycles, indicating the excellent reversibility of the $Ni_3(HATQ)_2$-based cathode. Significantly, reasonable selection of test procedures has a non-negligible effect on the electrochemical performance. As shown in Fig. S22,† the $Ni_3(HATQ)_2$-based cathode when charged to 3.6 V first shows higher initial capacity and better cycle performance than that discharged to 1.0 V, which might be attributed to the efficient intercalation of anions. In addition, a reasonable voltage range is crucial for stimulating capacity and maintaining stability. As shown in Fig. S23,† by comparing the different voltage ranges (1.0–3.5 V, 1.0–3.6 V and 1.0–3.8 V), it is clear that changing the upper limit of the voltage range can improve the capacity, but it may lead to the decomposition of the electrolyte, resulting in poor cycle stability. Furthermore, lowering the lower voltage limit can also increase the capacity, but the low voltage is not suitable for the cathode (Fig. S24†). In addition, decreasing mass loading also benefits the enhanced capacity (Fig. S25†).

Additionally, at 0.2 A g^{-1}, $Ni_3(HATQ)_2$ exhibits a reversible specific capacity of 115.1 mA h g^{-1} after 150 cycles (Fig. S26a†).Furthermore, compared with HATQ·6HCl, the $Ni_3(HATQ)_2$-based cathode exhibited superior redox ability and electrochemical performance (Fig. S26†). More importantly, the $Ni_3(HATQ)_2$-based cathode demonstrated distinctly superior

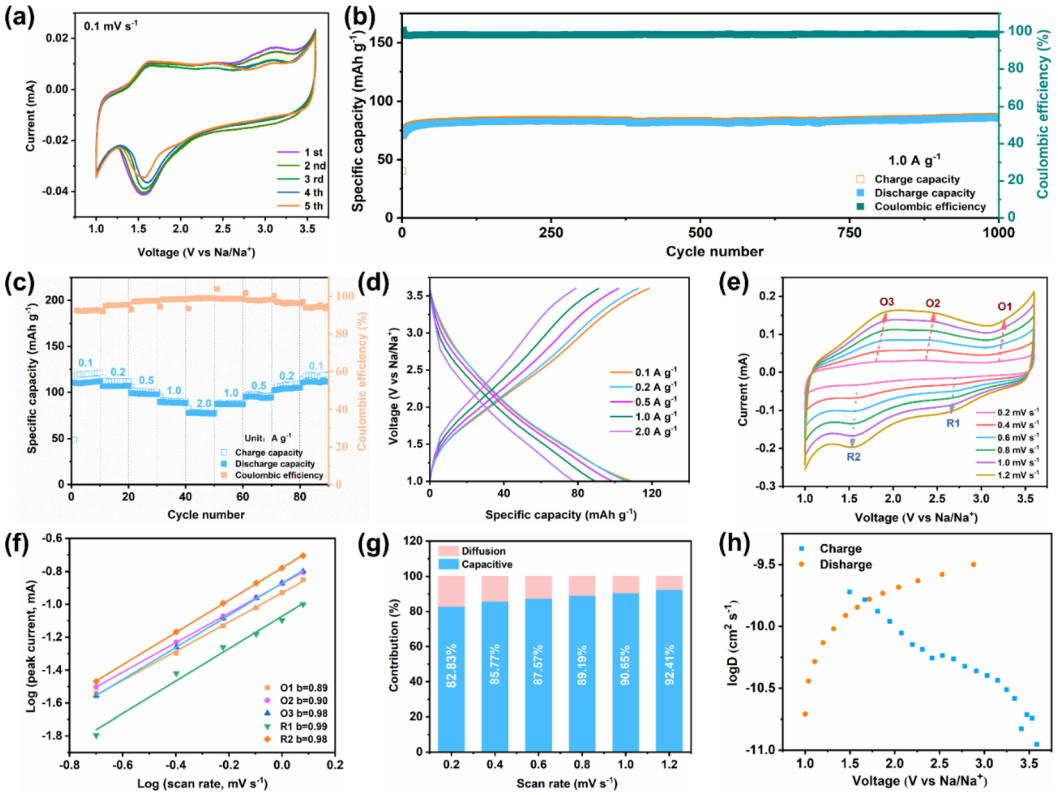

Fig. 3 Different electrochemical performances of the $Ni_3(HATQ)_2$ cathode in SIBs. (a) CV curves of $Ni_3(HATQ)_2$ at 0.1 mV s^{-1}. (b) Long-term cycling stability of $Ni_3(HATQ)_2$ measured at 1.0 A g^{-1}. (c) Rate capability of $Ni_3(HATQ)_2$. (d) GCD profiles of $Ni_3(HATQ)_2$ at different current densities. (e) CV curves of $Ni_3(HATQ)_2$ measured at different scan rates. (f) The relationship between logarithm peak current and the logarithm peak scan rate. (g) The percentage of diffusion and capacitive contributions at different scan rates. (h) Corresponding log D (D = Na^+ diffusion coefficient) at the discharge/charge state of $Ni_3(HATQ)_2$.

performance to $Ni_3(HITP)_2$ (ref. 45) at 1.0 A g^{-1} (Fig. S27†). Furthermore, the capacity of $Ni_3(HATQ)_2$ is superior to many other MOF-based cathodes and other inorganic cathodes (Table S2†) indicating the importance of electrode material selection and design. Fig. 3b shows that the excellent capacity retention (around 97%) and coulombic efficiency (CE) (nearly 100%) were retained at a higher current density of 1.0 A g^{-1} after 1000 cycles, revealing good long-term cycle stability. Moreover, the rate performance on the $Ni_3(HATQ)_2$ cathode was measured (Fig. 3c and d), with current densities ranging from 0.1 to 2.0 A g^{-1}. The discharge specific capacities were about 108.1, 105.7, 98.0, 88.6 and 77.1 mA h g^{-1}, respectively. Upon returning to a current density of 0.1 A g^{-1}, the capacity was recovered to 107.8 mA h g^{-1} with a restoration ratio of 99%. Furthermore, the reaction kinetics were analyzed through CV curves at different scan rates from 0.2 to 1.2 mV s^{-1}. As shown in Fig. 3e, the profiles of different CV curves are highly similar, while the corresponding peak area gradually increases when the scan rate aggrandizes.[46] According to the equation $i = av^b$, b values were determined by fitting the plot of log(i) and log(v) (see the ESI†). As shown in Fig. 3f, the calculated b values of O1, O2, O3, R1 and R2 were inclined to 1, revealing that the battery process is mainly controlled by capacitive behavior.

Furthermore, the ratio of diffusion to capacitive control is quantitatively analyzed using the Dunn equation. Fig. 3g and S28† show that the capacitive contribution is obviously increased with enhanced scan rates, and the ratio of capacitive control is up to 92.41% at a scan rate of 1.2 mV s^{-1}, indicating that the capacitive effect is the dominant contribution to battery capacity. Additionally, the Na^+ diffusion coefficient was determined by the galvanostatic intermittent titration technique (GITT), and the results showed that $Ni_3(HATQ)_2$ exhibits a high Na^+ diffusion coefficient (D) with log D values ranging from −9.0 to −11.0 cm^2 s^{-1} (Fig. 3h). These results indicate that $Ni_3(HATQ)_2$ features a fast kinetic process, which is beneficial for its electrochemical performance. Besides, Fig. S29† depicts the schematic diagram and electrochemical performance of the coin-type full cell when the anode is sodium terephthalate (Na_2TP), in which the Ni-TABQ||Na_2TP cell also shows desirable cycling performance with a reversible specific capacity of 56.3 mA h g^{-1} after 160 cycles at 0.2 A g^{-1}, indicating the feasibility of practical application.

To further understand the ion storage mechanism of $Ni_3(HATQ)_2$, *ex situ* FT-IR, XPS and EPR spectra were obtained to investigate the structural variation at selected voltage stages during charge/discharge processes (Fig. 4a). As shown in the *ex situ* FT-IR spectra in Fig. 4b, the corresponding peaks of the C–N bond gradually increased and the C=N bond stepwise weakened during discharge processes, indicating the generation of a C–N–Na group. Upon charging, the intensity of C–N bond

gradually diminished and C=N bond gradually enhanced. Specifically, evident peaks of PF_6^- (*ca.* 868 cm^{-1}) were detected in the *ex situ* FT-IR spectra at the charging state, revealing certain interaction between the anion and $Ni_3(HATQ)_2$ during the redox process.[30] To further confirm the transformation of the functional groups, XPS spectra were measured. The XPS spectra of N(1s) showed that C=N, C–N, and N-PF_6 exhibit similar variation tendencies with FT-IR spectra (Fig. 4c). Besides, the XPS P(2p) spectra exhibited an overwhelming signal upon charging to 3.6 V, which was distinguished from that of the discharge state (Fig. 4d). Compared with the pristine state, Ni(2p) spectra demonstrated negligible transformation during cycling (Fig. 4e), indicating that Ni(II) is immutable as a cathode material. These experimental data reveal co-storage of Na^+ and PF_6^- in $Ni_3(HATQ)_2$ during discharge/charge processes, which is beneficial for capacity promotion. The EPR signal increased during charging processes, which may be caused by the augmented the C=N bond (in the coordination center). In contrast, the signal peak decreased upon discharging to 1.0 V, indicating the generation of C–N–Na and formation of a radical intermediate during Na ion extraction/insertion processes (Fig. 4f). Moreover, these results indicate that the Na ion binding site is probably the coordinated nitrogen atoms instead of the Ni metal centers without valence state change. Meanwhile, Fig. S30† shows that the crystallinity of $Ni_3(HATQ)_2$ was well maintained at both charge and discharge states and the SEM image of charging to 2.8 V exhibited the intrinsic nanorod morphology, suggesting the structural stability of $Ni_3(HATQ)_2$ during the redox process.

To further investigate the co-storage mechanism of cations and anions, DFT calculations are conducted. The electronic band structure and density of states (DOS) reveal that $Ni_3(HATQ)_2$ possesses metallic electronic band structures, as evidenced by the non-zero density of states at Fermi energy (Fig. 5a).[47,48] This metallic property facilitates the transmission of electrons to the active sites. Additionally, molecular electrostatic potential (MESP) is determined to predict the possible active site for binding Na^+ and PF_6^-. The minimum value on the van der Waals surface (blue region) is centered at nitrogen elements, indicating that the C=N bond (coordination center) might attract Na ions more easily (Fig. 5b). In addition, $Ni_3(HATQ)_2$ exhibits heterogeneous charge distribution, with the N atoms of NiN_4 units being more negative than that of the TQ cores, which is beneficial for the preferential binding of Na ions. In contrast, the nitrogen elements of TQ ligand tend to act as the desirable active sites for binding PF_6^- (Fig. 5c). The subsequent differential charge explains that the charge density between $Ni_3(HATQ)_2$ and Na ions is increased, indicating a strong electronic interaction in the NiN_4 unit (Fig. 5d and S31†).[48] Meanwhile, the calculated binding energy verifies that Na^+ and PF_6^- are inclined to interact with the NiN_4 core and TQ motif, respectively. As well, the calculated reaction potentials of Na^+/PF_6^- intercalation are 1.00 V and 2.75 V, respectively, which correspond to the experimental potentials (Fig. 5e). Finally, the structural evolution progress is calculated to further confirm the redox site and the binding number of Na ions (Fig. 5f). The data indicate that six Na ions and two PF_6^- can be respectively extracted/inserted at the coordination bond and nitrogen

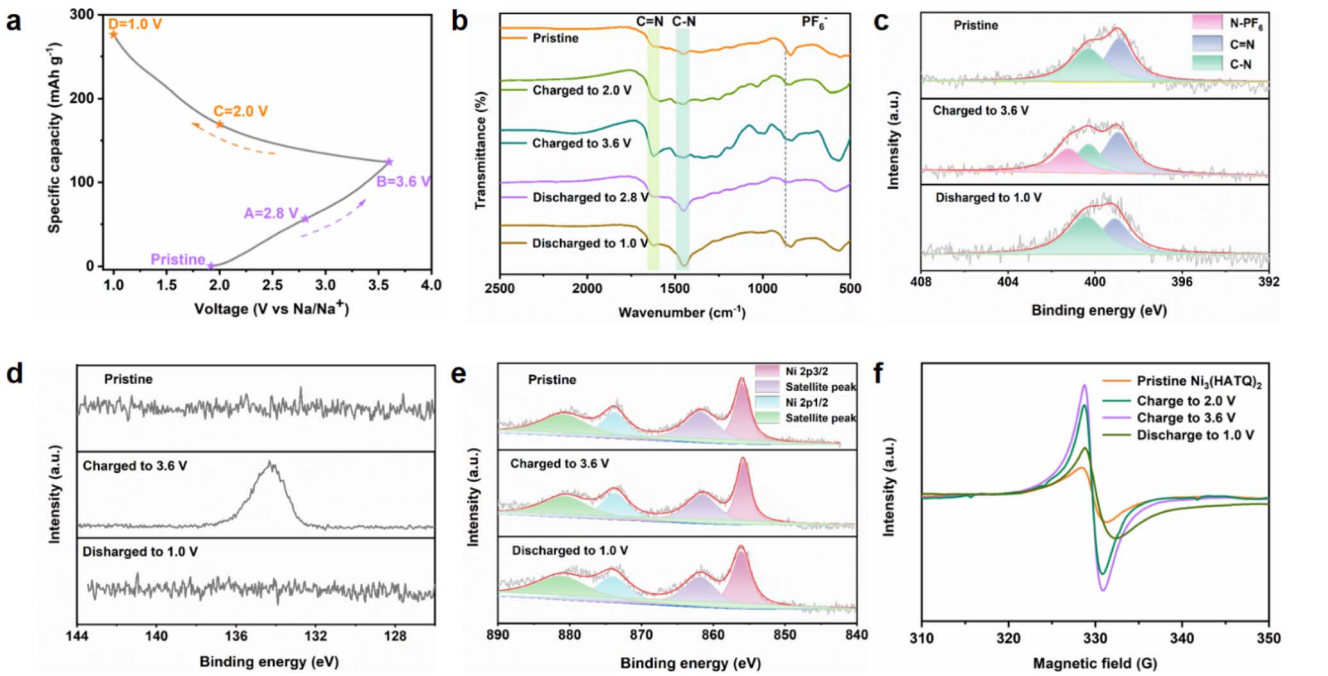

Fig. 4 XPS measurements and EPR spectra for investigating the ion storage mechanism of $Ni_3(HATQ)_2$. (a) Charge–discharge profiles and corresponding collections of voltage stages for *ex situ* investigation. (b) The *ex situ* FT-IR spectra. (c) The high resolution XPS N(1s) spectra. (d) The high resolution XPS P(2p) spectra. (e) The high resolution XPS Ni(2p) spectra and (f) EPR spectra of the $Ni_3(HATQ)_2$-based cathode at different charge and discharge voltages.

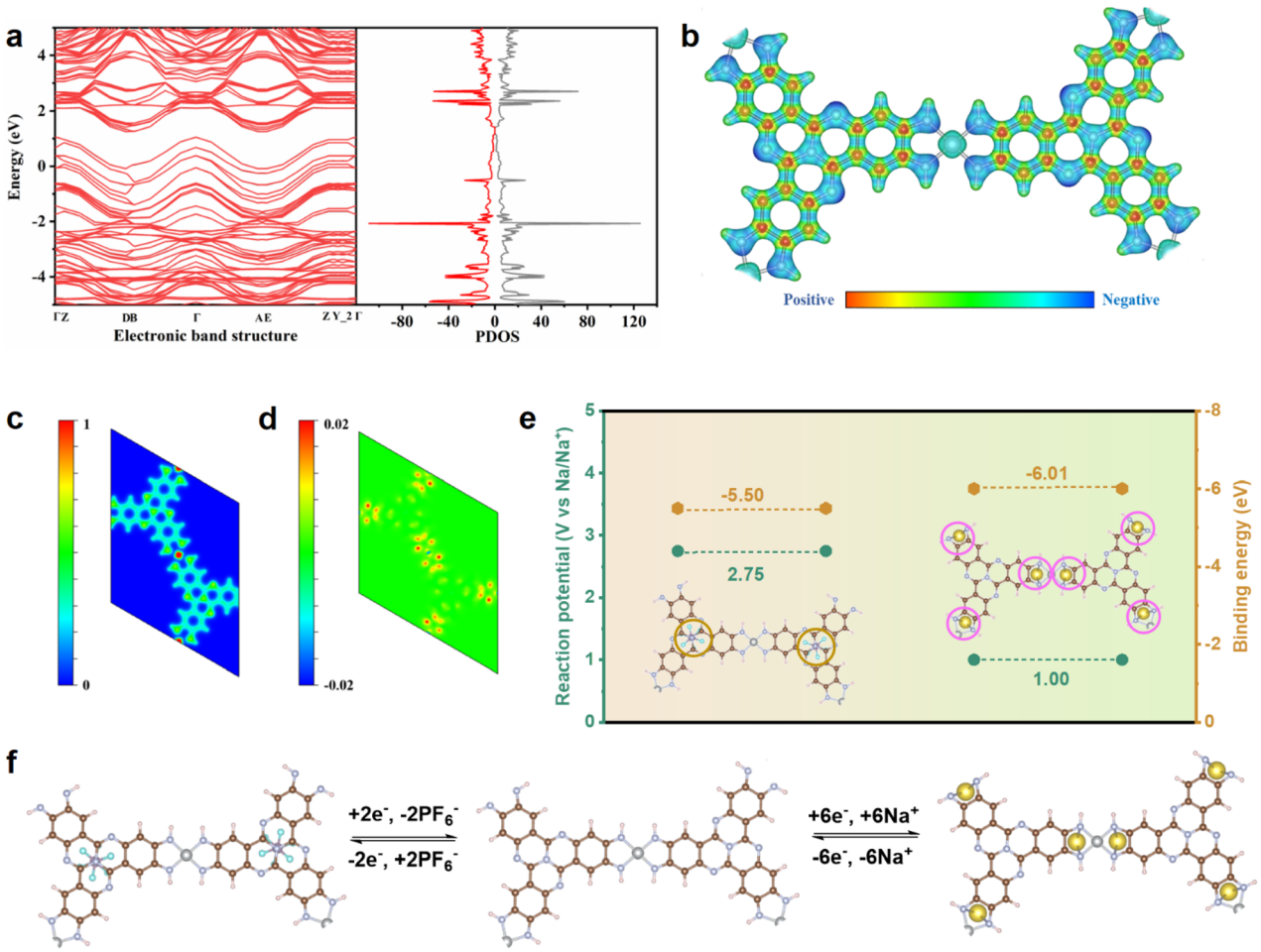

Fig. 5 DFT calculations for exploring the co-storage mechanism of cations and anions of $Ni_3(HATQ)_2$. (a) Electronic band structure and DOS of $Ni_3(HATQ)_2$. (b) MESP of the optimized cell of $Ni_3(HATQ)_2$. (c) The calculated 2D charge density. (d) Differential charge distribution of the $Ni_3(HATQ)_2$ repetitive unit. (e) The calculated reaction potential and binding energy of Na^+/PF_6^- interacting with different reaction sites based on $Ni_3(HATQ)_2$. (f) Structural evolution during the insertion/desertion of PF_6^- and sodium/de-sodium processes.

elements of the TQ ligand during the charge/discharge process based on the repetitive optimized cell. Overall, the calculated data are consistent with the experimental data and provide further insights into the cation and anion storage mechanism of $Ni_3(HATQ)_2$.

Conclusions

In summary, we successfully developed the facile synthesis of hexaaminotricycloquinazoline (HATQ) ligand as well as corresponding 2D *c*-MOF: $Ni_3(HATQ)_2$. Benefited by co-existence of p-type ligands (TQ) and an n-type coordination core (NiN_4), bipolar $Ni_3(HATQ)_2$ exhibits high discharge/charge capacities, excellent rate performance, and fast ion diffusion properties, when employed as a cathode material in SIBs. Moreover, 99% of the initial capacity retains after 150 cycles at a current density of 0.2 A g^{-1} and 95% of the restoration ratio at a higher current density of 1 A g^{-1} after 1000 cycles, revealing good long-term cycle stability. The experimental and theoretical results reveal that Na^+ binding sites are located on the N of NiN_4 linkages and the p-type TQ ligand could simultaneously accommodate PF_6^-. Overall, the current work highlights that reasonably developing novel p-type ligands to form functional 2D *c*-MOFs will provide a new pathway to simultaneously store cations and anions to further optimize battery performance.

Data availability

All experimental supporting data and procedures are available in the ESI.†

Author contributions

L. Chen conceived, designed, and guided the whole project; L. Q. Cheng and H. G. Wang performed the electrochemical experiments; D. Chen and W. B. Chen conducted the experiments and wrote the paper; F. C. Cui carried out the theoretical electrochemical calculation.

Conflicts of interest

There are no conflicts to declare.

Acknowledgements

This work was financially supported by the National Natural Science Foundation of China (51973153 and 52172186). The authors are grateful to have access to the beamline 4B9A of the Beijing Synchrotron Radiation Facility (BSRF).

References

1 L. Kong, M. Liu, H. Huang, Y. Xu and X.-H. Bu, *Adv. Energy Mater.*, 2022, **12**, 2100172.
2 J. Li, X. Jing, Q. Li, S. Li, X. Gao, X. Feng and B. Wang, *Chem. Soc. Rev.*, 2020, **49**, 3565–3604.
3 G. Zhou, L. Xu, G. Hu, L. Mai and Y. Cui, *Chem. Rev.*, 2019, **119**, 11042–11109.
4 P. Zhang, F. Wang, M. Yu, X. Zhuang and X. Feng, *Chem. Soc. Rev.*, 2018, **47**, 7426–7451.
5 J.-Y. Hwang, S.-T. Myung and Y.-K. Sun, *Chem. Soc. Rev.*, 2017, **46**, 3529–3614.
6 Y. Huang, L. Zhao, L. Li, M. Xie, F. Wu and R. Chen, *Adv. Mater.*, 2019, **31**, 1808393.
7 P. K. Nayak, L. Yang, W. Brehm and P. Adelhelm, *Angew. Chem., Int. Ed.*, 2018, **57**, 102–120.
8 S.-W. Kim, D.-H. Seo, X. Ma, G. Ceder and K. Kang, *Adv. Energy Mater.*, 2012, **2**, 710–721.
9 Q. Zhao, A. K. Whittaker and X. S. Zhao, *Mater*, 2018, **11**, 2567.
10 X. Yin, S. Sarkar, S. Shi, Q.-A. Huang, H. Zhao, L. Yan, Y. Zhao and J. Zhang, *Adv. Funct. Mater.*, 2020, **30**, 1908445.
11 M. D. Allendorf, R. Dong, X. Feng, S. Kaskel, D. Matoga and V. Stavila, *Chem. Rev.*, 2020, **120**, 8581–8640.
12 M. Wang, R. Dong and X. Feng, *Chem. Soc. Rev.*, 2021, **50**, 2764–2793.
13 M. Hmadeh, Z. Lu, Z. Liu, F. Gándara, H. Furukawa, S. Wan, V. Augustyn, R. Chang, L. Liao, F. Zhou, E. Perre, V. Ozolins, K. Suenaga, X. Duan, B. Dunn, Y. Yamamto, O. Terasaki and O. M. Yaghi, *Chem. Mater.*, 2012, **24**, 3511–3513.
14 X. Huang, S. Zhang, L. Liu, L. Yu, G. Chen, W. Xu and D. Zhu, *Angew. Chem., Int. Ed.*, 2018, **57**, 146–150.
15 Z. Wu, J. Xie, Z. J. Xu, S. Zhang and Q. Zhang, *J. Mater. Chem. A*, 2019, **7**, 4259–4290.
16 C. Cong and H. Ma, *Small*, 2023, **19**, 2207547.
17 M. Wang, H. Shi, P. Zhang, Z. Liao, M. Wang, H. Zhong, F. Schwotzer, A. S. Nia, E. Zschech, S. Zhou, S. Kaskel, R. Dong and X. Feng, *Adv. Funct. Mater.*, 2020, **30**, 2002664.
18 Y. Lu, Y. Zhang, C.-Y. Yang, S. Revuelta, H. Qi, C. Huang, W. Jin, Z. Li, V. Vega-Mayoral, Y. Liu, X. Huang, D. Pohl, M. Položij, S. Zhou, E. Cánovas, T. Heine, S. Fabiano, X. Feng and R. Dong, *Nat. Commun.*, 2022, **13**, 7240.
19 D. Feng, T. Lei, M. R. Lukatskaya, J. Park, Z. Huang, M. Lee, L. Shaw, S. Chen, A. A. Yakovenko, A. Kulkarni, J. Xiao, K. Fredrickson, J. B. Tok, X. Zou, Y. Cui and Z. Bao, *Nat. Energy*, 2018, **3**, 30–36.
20 C. Qian, Q.-Y. Qi, G.-F. Jiang, F.-Z. Cui, Y. Tian and X. Zhao, *J. Am. Chem. Soc.*, 2017, **139**, 6736–6743.
21 L. S. Xie, G. Skorupskii and M. Dincă, *Chem. Rev.*, 2020, **120**, 8536–8580.
22 D. Herebian, E. Bothe, F. Neese, T. Weyhermüller and K. Wieghardt, *J. Am. Chem. Soc.*, 2003, **125**, 9116–9128.
23 D. Sheberla, L. Sun, M. A. Blood-Forsythe, S. Er, C. R. Wade, C. K. Brozek, A. Aspuru-Guzik and M. Dincă, *J. Am. Chem. Soc.*, 2014, **136**, 8859–8862.
24 G. Wu, J. Huang, Y. Zang, J. He and G. Xu, *J. Am. Chem. Soc.*, 2017, **139**, 1360–1363.
25 M. G. Campbell, S. F. Liu, T. M. Swager and M. Dincă, *J. Am. Chem. Soc.*, 2015, **137**, 13780–13783.
26 B. Wang, J. Li, M. Ye, Y. Zhang, Y. Tang, X. Hu, J. He and C. C. Li, *Adv. Funct. Mater.*, 2022, **32**, 2112072.
27 F. Wang, Z. Liu, C. Yang, H. Zhong, G. Nam, P. Zhang, R. Dong, Y. Wu, J. Cho, J. Zhang and X. Feng, *Adv. Mater.*, 2020, **32**, 1905361.
28 Y. Chen, Q. Zhu, K. Fan, Y. Gu, M. Sun, Z. Li, C. Zhang, Y. Wu, Q. Wang, S. Xu, J. Ma, C. Wang and W. Hu, *Angew. Chem., Int. Ed.*, 2021, **60**, 18769–18776.
29 L. Wang, Y. Ni, X. Hou, L. Chen, F. Li and J. Chen, *Angew. Chem., Int. Ed.*, 2020, **59**, 22126–22131.
30 Q. Jiang, P. Xiong, J. Liu, Z. Xie, Q. Wang, X.-Q. Yang, E. Hu, Y. Cao, J. Sun, Y. Xu and L. Chen, *Angew. Chem., Int. Ed.*, 2020, **59**, 5273–5277.
31 J. Yin, N. Li, M. Liu, Z. Li, X. Wang, M. Cheng, M. Zhong, W. Li, Y. Xu and X.-H. Bu, *Adv. Funct. Mater.*, 2023, **33**, 2211950.
32 O. Buyukcakir, R. Yuksel, Y. Jiang, S. H. Lee, W. K. Seong, X. Chen and R. S. Ruoff, *Angew. Chem., Int. Ed.*, 2019, **58**, 872–876.
33 J.-H. Dou, M. Q. Arguilla, Y. Luo, J. Li, W. Zhang, L. Sun, J. L. Mancuso, L. Yang, T. Chen, L. R. Parent, G. Skorupskii, N. J. Libretto, C. Sun, M. C. Yang, P. V. Dip, E. J. Brignole, J. T. Miller, J. Kong, C. H. Hendon, J. Sun and M. Dincă, *Nat. Mater.*, 2021, **20**, 222–228.
34 J. Liu, D. Yang, Y. Zhou, G. Zhang, G. Xing, Y. Liu, Y. Ma, O. Terasaki, S. Yang and L. Chen, *Angew. Chem., Int. Ed.*, 2021, **60**, 14473–14479.
35 J. Yan, Y. Cui, M. Xie, G.-Z. Yang, D.-S. Bin and D. Li, *Angew. Chem., Int. Ed.*, 2021, **60**, 24467–24472.
36 Z. Yang, T. Wang, H. Chen, X. Suo, P. Halstenberg, H. Lyu, W. Jiang, S. M. Mahurin, I. Popovs and S. Dai, *ACS Energy Lett.*, 2021, **6**, 41–51.
37 L. Chen, J. Kim, T. Ishizuka, Y. Honsho, A. Saeki, S. Seki, H. Ihee and D. Jiang, *J. Am. Chem. Soc.*, 2009, **131**, 7287–7292.
38 H. Bahron, S. S. Khaidir, A. M. Tajuddin, K. Ramasamy and B. M. Yamin, *Polyhedron*, 2019, **161**, 84–92.
39 V. Torabi, H. Kargar, A. Akbari, R. Behjatmanesh-Ardakani, H. Amiri Rudbari and M. Nawaz Tahir, *J. Coord. Chem.*, 2018, **71**, 3748–3762.
40 Y. Jiang, I. Oh, S. H. Joo, O. Buyukcakir, X. Chen, S. H. Lee, M. Huang, W. K. Seong, S. K. Kwak, J.-W. Yoo and R. S. Ruoff, *J. Am. Chem. Soc.*, 2019, **141**, 16884–16893.
41 Y. Yue, P. Cai, X. Xu, H. Li, H. Chen, H.-C. Zhou and N. Huang, *Angew. Chem., Int. Ed.*, 2021, **60**, 10806–10813.

42 J. Xu, W. Zhang, D. Geng, Y. Liu, H. Wang, N. Tang and G. Yu, *Adv. Electron. Mater.*, 2015, **1**, 1500084.
43 C. Li, W. Ju, S. Vijay, J. Timoshenko, K. Mou, D. A. Cullen, J. Yang, X. Wang, P. Pachfule, S. Brückner, H. S. Jeon, F. T. Haase, S.-C. Tsang, C. Rettenmaier, K. Chan, B. R. Cuenya, A. Thomas and P. Strasser, *Angew. Chem., Int. Ed.*, 2022, **61**, e202114707.
44 J.-D. Yi, D.-H. Si, R. Xie, Q. Yin, M.-D. Zhang, Q. Wu, G.-L. Chai, Y.-B. Huang and R. Cao, *Angew. Chem., Int. Ed.*, 2021, **60**, 17108–17114.
45 T. Chen, J.-H. Dou, L. Yang, C. Sun, N. J. Libretto, G. Skorupskii, J. T. Miller and M. Dincă, *J. Am. Chem. Soc.*, 2020, **142**, 12367–12373.
46 H. Li, M. Tang, Y. Wu, Y. Chen, S. Zhu, B. Wang, C. Jiang, E. Wang and C. Wang, *J. Phys. Chem. Lett.*, 2018, **9**, 3205–3211.
47 Y.-X. Liu, H. Zhang and X.-L. Cheng, *Chem. Phys.*, 2023, **568**, 111837.
48 H.-g. Wang, Q. Li, Q. Wu, Z. Si, X. Lv, X. Liang, H. Wang, L. Sun, W. Shi and S. Song, *Adv. Energy Mater.*, 2021, **11**, 2100381.